

Hierarchical Multi-Modal Planning for Fixed-Altitude Sparse Target Search and Sampling

Lingpeng Chen, Yuchen Zheng, Apple Pui-Yi Chui, Junfeng Wu and Ziyang Hong

Abstract—Efficient monitoring of sparse benthic phenomena, such as coral colonies, presents a great challenge for Autonomous Underwater Vehicles. Traditional exhaustive coverage strategies are energy-inefficient, while recent adaptive sampling approaches rely on costly vertical maneuvers. To address these limitations, we propose HIMoS (Hierarchical Informative Multi-Modal Search), a fixed-altitude framework for sparse coral search-and-sample missions. The system integrates a heterogeneous sensor suite within a two-layer planning architecture. At the strategic level, a Global Planner optimizes topological routes to maximize potential discovery. At the tactical level, a receding-horizon Local Planner leverages differentiable belief propagation to generate kinematically feasible trajectories that balance acoustic substrate exploration, visual coral search, and close-range sampling. Validated in high-fidelity simulations derived from real-world coral reef benthic surveys, our approach demonstrates superior mission efficiency compared to state-of-the-art baselines.

I. INTRODUCTION

Efficient monitoring of sparse benthic phenomena, such as corals, invasive species, or rare biological aggregations, is a critical challenge for autonomous underwater vehicles (AUVs) [1]. Unlike continuous scalar fields (e.g., salinity or temperature) that can be mapped using standard spatiotemporal models [2], [3], biological targets are intrinsically discrete and sparsely distributed. Traditional exhaustive coverage strategies, such as lawnmower paths [4], [5], are highly energy-inefficient in these scenarios, wasting limited battery life on traversing vast, empty stretches of the seabed.

Recent informative path planning and adaptive sampling methods [6], [7] vary sensor coverage by oscillating between high-altitude visual scouting and low-altitude target sampling; this idea is exemplified by the Sparse Adaptive Search and Sample (SASS) algorithm [8], which has been applied to coral sampling. However, these methods face significant hurdles in realistic ocean deployments. Physically, frequent vertical maneuvering is highly energy-intensive, and reliance on high-altitude vision is brittle in turbid marine environments (e.g., Shenzhen coastal waters, Fig. 1), where light scattering severely limits optical range. Algorithmically, state-of-the-art frameworks often rely on grid-based discrete planners like Monte Carlo Tree Search [8], which scale poorly with map resolution and struggle to yield kinematically feasible trajectories. This highlights a pressing need for a fixed-altitude framework that seamlessly couples long-range robust acoustics [9], [10] with close-range vision, driven by a scalable and kinematically-aware planning architecture.

To overcome these challenges, we propose HIMoS (Hierarchical Informative Multi-Modal Search), a robust framework tailored for sparse search-and-sample (SSS) mis-

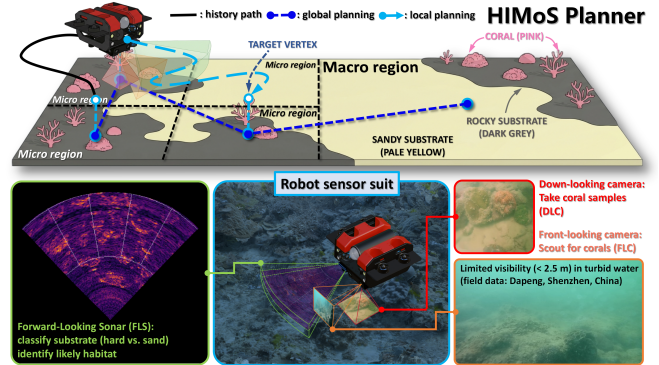


Fig. 1: HIMoS overview. *Bottom*: multi-modal sensing for turbid ocean. *Top*: hierarchical planning framework steers the AUV to high-probability coral habitats for sampling.

sions. Operating safely at a fixed altitude, HIMoS eliminates the need for energy-intensive vertical maneuvers. Instead, it overcomes turbid marine conditions by seamlessly fusing a heterogeneous sensor suite: a Forward-Looking Sonar (FLS) provides broad-area acoustic substrate mapping [11], [12], a Front-Looking Camera (FLC) enables mid-range target scouting, and a Down-Looking Camera (DLC) executes precise close-range sampling. As illustrated in Fig. 1, this multi-modal synergy empowers the AUV to rapidly bypass vast, uninhabitable sandy regions and zero in on high-probability hard substrates where corals typically reside [13].

Algorithmically, HIMoS is driven by a hierarchical architecture that seamlessly couples long-horizon strategic routing with agile local maneuvering. At the strategic level, a Global Planner identifies the most promising target regions under a strict travel budget. We cast this decision as an orienteering problem and rank candidate regions using an Upper Confidence Bound (UCB) utility that rewards both high predicted habitat probability and high epistemic uncertainty, thereby balancing exploitation and exploration. At the tactical level, a receding-horizon Local Planner translates these global directives into execution. To fuse heterogeneous sensors (FLS, FLC, and DLC), we introduce *Differentiable Belief Dynamics* to continuously simulate the future evolution of stochastic sensor updates. By embedding these dynamics into a unified objective function, the planner generates smooth, kinematically feasible trajectories that optimally trade off multi-modal map entropy reduction (exploration) and precise visual target sampling (exploitation).

Our main contributions are threefold. First, we propose a *hierarchical global-local planning architecture* that integrates a strategic orienteering-based Global Planner with a receding-horizon Local Planner, achieving mission-level

efficiency while retaining local agility. Second, we formulate local informative planning as a gradient-based trajectory optimization problem via *Differentiable Belief Dynamics*. By employing a continuous surrogate for stochastic sensor updates, the planner generates kinematically feasible and non-myopic trajectories that seamlessly balance broad-area exploration with close-range target sampling. Third, we present *seamless heterogeneous sensor fusion*, a unified strategy that combines acoustic and visual data to support efficient fixed-altitude sparse target search and sampling in ocean environments.

II. PROBLEM FORMULATION

We formulate the SSS mission as a multi-sensor informative path planning (IPP) problem. Consider an AUV operating in an 2D unknown ocean environment \mathcal{M} and aim to maximize the number of sampled coral targets under a time budget T_{total} (second).

The environment \mathcal{M} is discretized into a grid map consisting of N cells, indexed by i . Each cell possesses two latent binary states. **Substrate state** $s_i \in \{0, 1\}$ indicates habitability, where $s_i = 1$ denotes hard substrate and $s_i = 0$ denotes uninhabitable substrate (e.g., sand). **Target state** $c_i \in \{0, 1\}$ indicates the presence of a coral target, where $c_i = 1$ denotes presence.

The AUV operates at a fixed altitude suitable for benthic surveying, so the configuration space is restricted to Special Euclidean group $SE(2)$. At discrete planning step t , the robot state is $\mathbf{x}_t = [\mathbf{p}_t^\top, \theta_t]^\top \in SE(2)$, where $\mathbf{p}_t \in \mathbb{R}^2$ represents the position and θ_t represents the heading. The AUV system evolves according to discrete-time holonomic kinematics $\mathbf{x}_{t+1} = f(\mathbf{x}_t, \mathbf{u}_t)$ with continuous control input $\mathbf{u}_t = [v_{x,t}, v_{y,t}, \omega_t]^\top \in \mathcal{U}$, where \mathcal{U} denotes the admissible control set (surge, sway, and yaw rate).

A. Heterogeneous Observation Models

As motivated in Sec. I and illustrated in Fig. 1, the AUV is equipped with a heterogeneous sensor suite to effectively navigate turbid marine environments. To mathematically formalize their complementary roles—namely, wide-range acoustic habitat mapping (FLS), mid-range visual target scouting (FLC), and close-range coral sampling (DLC)—we categorize the three distinct modalities into *Probabilistic Scouting Sensors* and a *Deterministic Verification Sensor*.

1) *Probabilistic Scouting Sensors*: The FLS and FLC are tasked with gathering long-range evidence of habitats and mid-range evidence of targets, respectively. Because signal reliability inherently degrades with distance, these sensors provide noisy, range-dependent measurements over a sector-shaped Field-of-View (FOV). Let $\mathcal{V}(\mathbf{x}_t, \Theta)$ denote the set of cells visible to a sensor at robot state \mathbf{x}_t , where $\Theta = \{R_{\max}, \phi_{\text{fov}}\}$ specifies the maximum sensing range R_{\max} and the FOV angular span ϕ_{fov} . For a cell i centered at $\mathbf{p}_i \in \mathcal{V}(\mathbf{x}_t, \Theta)$, the binary observation $z_{t,i} \in \{0, 1\}$ is modeled using a probabilistic detection model parameterized by the True Positive (P_{TP}) and False Positive (P_{FP}) rates [14]. We assume these rates are functions of the robot-to-cell distance

$d_{t,i} = \|\mathbf{p}_t - \mathbf{p}_i\|$ (with \mathbf{p}_t the robot position), and their profiles are known *a priori* (e.g. via sensor calibration):

$$P(z_{t,i} = 1 \mid \text{state}_i) = \begin{cases} P_{\text{TP}}(d_{t,i}) & \text{if } \text{state}_i(s_i/c_i) = 1 \\ P_{\text{FP}}(d_{t,i}) & \text{if } \text{state}_i = 0. \end{cases} \quad (1)$$

We instantiate this general stochastic model for our two scouting modalities: the FLS observes the substrate state s_i , while the FLC observes the target state c_i .

2) *Deterministic Verification Sensor*: The DLC provides close-range verification for coral sampling with a small footprint $\mathcal{V}_{\text{DLC}}(\mathbf{x}_t)$ beneath the robot. At this proximity, we model DLC observations as noise-free and deterministic:

$$z_{t,j}^{\text{DLC}} = c_j, \quad \forall j \in \mathcal{V}_{\text{DLC}}(\mathbf{x}_t). \quad (2)$$

Crucially, a target is counted as **sampled** (yields reward) if and only if it is observed by the DLC.

B. Environmental Prior and Belief Dynamics

The existence of a target is governed by a strong biological prior: corals exclusively inhabit hard substrates [13]. We model this as a conditional probability constraint $P(c_i = 1 \mid s_i = 0) = 0$. Consequently, the joint probability of finding a coral is strictly coupled with the substrate probability: $P(c_i = 1) = P(c_i = 1 \mid s_i = 1)P(s_i = 1)$. Initially, the true map layers $\{s_i\}_{i=1}^N$ and $\{c_i\}_{i=1}^N$ are unknown to the robot. To reflect this initial uncertainty, the environment is initialized with uninformative prior probabilities (e.g., uniform distributions $P(s_i = 1) = 0.5$ and $P(c_i = 1 \mid s_i = 1) = 0.5$). Since the true states remain hidden, the robot maintains a probabilistic *belief state* over \mathcal{M} at each discrete time step t . We define this belief state as $\mathcal{B}_t = \{\mathcal{B}_t^S, \mathcal{B}_t^C\}$, where $\mathcal{B}_{t,i}^S = P(s_i = 1 \mid z_{1:t}^{\text{FLS}})$ is the posterior probability of the substrate type given historical acoustic observations. $\mathcal{B}_{t,i}^C = P(c_i = 1 \mid z_{1:t}^{\text{FLC}})$ is the posterior probability of coral existence given historical visual observations.

These beliefs are updated via Bayesian filtering with new scouting measurements. For numerical stability, we use a log-odds form [14]. Let $b_{t,i} = P(\text{state}_i = 1 \mid z_{1:t})$ and $\ell_{t,i} = \log \frac{b_{t,i}}{1-b_{t,i}}$. Based on Eq. (1), given a binary scouting measurement $z_{t,i} \in \{0, 1\}$, the log-odds update is¹

$$\ell_{t,i} = \ell_{t-1,i} + \log \frac{P_{\text{TP}}(d_{t,i})^{z_{t,i}}(1 - P_{\text{TP}}(d_{t,i}))^{1-z_{t,i}}}{P_{\text{FP}}(d_{t,i})^{z_{t,i}}(1 - P_{\text{FP}}(d_{t,i}))^{1-z_{t,i}}}. \quad (3)$$

Intuitively, as the belief distributions converge and uncertainty diminishes, the robot can exploit the substrate belief map B^S to find high-yield regions and transform ambiguous coral belief maps B^C into confident coral sampling targets.

C. Optimization Objective

We seek a control sequence $\mathbf{U}^* = \{\mathbf{u}_0^*, \dots, \mathbf{u}_{T-1}^*\}$ that maximizes the number of targets sampled by the DLC. To avoid double-counting, we maintain a binary history mask $\xi_t \in \{0, 1\}^N$ indicating cells previously covered by the DLC.

¹For deterministic DLC measurement (Eq. (2)), the posterior becomes deterministic; therefore we saturate the log-odds to $[\ell_{\min}, \ell_{\max}]$.

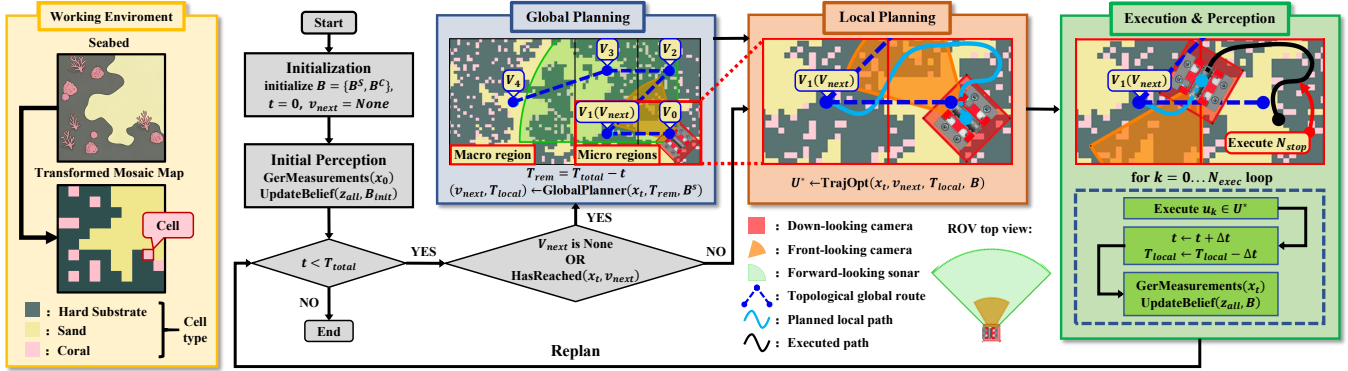


Fig. 2: System overview. An event-triggered Global Planner produces the next target region v_{next} and local budget T_{local} . A time-triggered Local Planner receives them and optimizes a finite-horizon trajectory based on belief \mathcal{B} . The robot then executes the trajectory for N_{exec} steps while collecting measurements and updating the belief, after which HIMoS re-plans.

The task is formulated as maximizing the cumulative reward (count of sampled corals) under the time budget T_{total} :

$$\mathbf{U}^* = \arg \max_{\mathbf{u}_{0:T-1} \in \mathcal{U}^T} \mathbb{E}_{\mathcal{B}} \left[\sum_{k=1}^T \sum_{j \in \mathcal{V}_{DLC}(\mathbf{x}_k)} c_j \cdot (1 - \xi_{k-1,j}) \right] \quad (4)$$

$$\text{s.t. } \mathbf{x}_{k+1} = f(\mathbf{x}_k, \mathbf{u}_k, \Delta t), \quad T \cdot \Delta t \leq T_{total},$$

where $\mathbb{E}_{\mathcal{B}}$ is taken over the scouting beliefs $(\mathcal{B}^S, \mathcal{B}^C)$, which steer the DLC toward high-probability targets.

III. SYSTEM OVERVIEW

Directly maximizing the expected sampling reward in Eq. (4) is computationally intractable. To make this objective solvable while strictly satisfying T_{total} , we design HIMoS shown in Fig. 2, a hierarchical framework that spatially and temporally decomposes the overarching problem.

Operating in an online closed-loop manner, HIMoS bridges long-term strategic routing with short-term tactical execution. At the strategic level, an event-triggered Global Planner—activated whenever the AUV successfully reaches its current target region v_{next} (*HasReached*) and requires new global guidance—approximates Eq. (4) by evaluating the remaining time and the latest substrate belief \mathcal{B}^S to solve a topological Orienteering Problem (OP) (Sec. IV). This abstracts the global search space, generating a route across high-probability habitats. Instead of executing the entire route, the planner extracts the first OP node as the immediate target region v_{next} and allocates a local time budget T_{local} to constrain the subsequent tactical maneuvers.

At the tactical level, a time-triggered Local Planner translates this directive into kinematically feasible maneuvers toward v_{next} . To bypass the non-differentiability of stochastic observations, we introduce Differentiable Belief Dynamics (Sec. V). This surrogate model casts the finite-horizon information search and sample as a smooth Non-Linear Programming (NLP) problem bounded by T_{local} . Operating in a receding-horizon fashion, the AUV executes only the first N_{exec} steps, continuously acquiring observations to update the belief map $\mathcal{B} = \{\mathcal{B}^S, \mathcal{B}^C\}$. This tightly coupled sense-update-replan loop persists locally until v_{next}

is reached, which triggers the next global guidance and naturally chains local executions into global milestones. This grounds every decision in the most recent perceptual evidence, enhancing overall mission efficiency and robustness against noise in turbid environments.

IV. GLOBAL PLANNING: TOPOLOGICAL ROUTE GENERATION

To guide the AUV toward high-potential habitats under a strict time budget, the Global Planner formulates an Orienteering Problem (OP) over the FLS-updated substrate belief \mathcal{B}^S . As outlined in Alg. 1, this process comprises three stages: (1) constructing an adaptive spatial graph from \mathcal{B}^S , (2) modeling a continuous reward field via a Heteroscedastic Gaussian Process (GP), and (3) solving the OP to output the next target node v_{next} and a local time budget T_{local} .

A. Adaptive Multi-Resolution Spatial Graph and Node Aggregation

To balance decision quality and real-time tractability, we construct a multi-resolution graph $\mathcal{G} = (\mathcal{V}, \mathcal{E})$, whose node resolution is modulated by the FLS coverage encoded in \mathcal{B}^S .

1) *Hierarchical Workspace Decomposition*: We initialize the workspace with coarse macro regions, represented by their centroids as a node set \mathcal{V}_{macro} . This keeps the OP tractable during early, sparse exploration. As acoustic coverage accumulates, if the FLS observation reduces the aggregated posterior uncertainty of a macro region below a predefined threshold (Fig. 3), the region is subdivided into finer micro regions. Their centroids form the micro node set \mathcal{V}_{micro} . The resulting heterogeneous node set $\mathcal{V}_{opt} =$

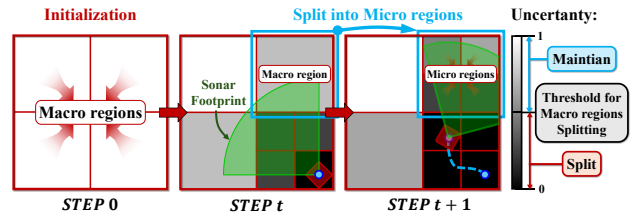


Fig. 3: Adaptive Macro region splitting process. When FLS gathers enough evidence to reduce a region’s substrate uncertainty below a threshold, the corresponding Macro region is divided into Micro regions to enable high-fidelity planning.

Algorithm 1: Global Planner

Input : State \mathbf{x}_t , Substrate Belief \mathcal{B}^S , Time T_{rem}
Output: Target v_{next} , Local Budget T_{local}
State : $\mathcal{V}_{macro} \leftarrow \text{Init}(\mathcal{M})$, $\mathcal{V}_{micro} \leftarrow \emptyset$
// -- 1. Construct graph --
1 **foreach** $v \in \mathcal{V}_{macro}$ **do**
2 **if** $\text{IsBlockObserved}(v, \mathcal{B}_t^S)$ **then**
3 $\mathcal{V}_{macro} \leftarrow \mathcal{V}_{macro} \setminus \{v\}$
4 $\mathcal{V}_{micro} \leftarrow \mathcal{V}_{micro} \cup \text{SplitMacroBlock}(v)$
5 $\mathcal{V}_{opt} \leftarrow \mathcal{V}_{macro} \cup \mathcal{V}_{micro}$
// -- 2. Learn Reward Field --
6 $\mathcal{D} \leftarrow \text{AggregateNodeStats}(\mathcal{V}_{micro}, \mathcal{B}_t^S)$
7 $GP \leftarrow \text{TrainGP}(\mathcal{D})$
8 **foreach** $v_i \in \mathcal{V}_{opt}$ **do**
9 $r_i \leftarrow \text{CalcInfoReward}(GP, v_i)$
// -- 3. Solve OP --
10 $D_{rem} \leftarrow T_{rem}/c$ // Map time to distance budget
11 $\pi^* \leftarrow \text{SolveOP}(\mathcal{V}_{opt}, \{r_i\}, D_{rem})$
12 $v_{next} \leftarrow \pi^*.pop()$ $e_{next} \leftarrow \text{Dist}(\mathbf{x}_t, v_{next})$
13 $T_{local} \leftarrow c \cdot \|e_{next}\|$ // Map back to tactical time
14 **return** v_{next}, T_{local}

$\mathcal{V}_{macro} \cup \mathcal{V}_{micro}$ maintains broad, low-resolution nodes in unexplored areas while incorporating high-fidelity nodes for exploitation in confidently surveyed regions.

2) *Probabilistic Node Aggregation*: We extract node-level statistics from the belief map \mathcal{B}_t^S for the graph-based planner (Line 6). For each micro node $v_i \in \mathcal{V}_{micro}$ representing a spatial region \mathcal{R}_i centered at $\mathbf{p}_i \in \mathbb{R}^2$, We aggregate the local substrate density $\bar{\rho}_i$ and its associated observation uncertainty \bar{v}_i^2 by spatially averaging the belief mean and variance over grid cells $j \in \mathcal{R}_i$, i.e., $\bar{\rho}_i = \mathbb{E}_{j \in \mathcal{R}_i}[B_j^S]$ and $\bar{v}_i^2 = \mathbb{E}_{j \in \mathcal{R}_i}[\text{Var}(B_j^S)]$. This aggregation effectively compresses dense map beliefs into a compact graph representation $\mathcal{D} = \{(\mathbf{p}_i, \bar{\rho}_i, \bar{v}_i^2)\}$ to train the heteroscedastic Gaussian Process.

B. Heteroscedastic Substrate Modeling

To guide the robot toward promising habitats, we model the latent substrate density field as a continuous function. Because the reliability of acoustic measurements inherently degrades with sensing range, we employ a heteroscedastic Gaussian Process (GP) to rigorously account for spatially varying observation noise [15]. Trained on the aggregated graph statistics \mathcal{D} , the GP constructs an observation noise matrix $\mathbf{R} = \text{diag}(\bar{v}_1^2, \dots, \bar{v}_M^2)$ that explicitly injects each node’s input-dependent uncertainty. For any candidate node v_i at \mathbf{p}_i , the posterior predictive mean and variance are computed directly as $\mu_i = \mathbf{k}_i^\top (\mathbf{K} + \mathbf{R})^{-1} \bar{\boldsymbol{\rho}}$ and $\sigma_i^2 = k(\mathbf{p}_i, \mathbf{p}_i) - \mathbf{k}_i^\top (\mathbf{K} + \mathbf{R})^{-1} \mathbf{k}_i$, respectively, where \mathbf{K} is the training covariance matrix, \mathbf{k}_i is the cross-covariance vector, and $\bar{\boldsymbol{\rho}} = [\bar{\rho}_1, \dots, \bar{\rho}_M]^\top$. Consequently, sparsely observed regions naturally exhibit high predictive variance σ_i^2 to drive exploration, whereas thoroughly scanned regions are

“pinned” with low variance for confident exploitation.

C. Decision Making: The Orienteering Problem

At each global replanning step t , we determine the next strategic waypoint v_{next} on the adaptive graph $\mathcal{G}_t = (\mathcal{V}_t, \mathcal{E}_t)$ by formulating a Budgeted Orienteering Problem (OP) [16]. To balance the exploitation of high substrate density regions against the exploration of unknown regions, we assign a composite reward r_i to each candidate node v_i :

$$r_i = (\mu_i + \beta \sigma_i) \cdot \lambda_i^{area} \cdot \mathbb{I}(v_i \notin \mathcal{V}_{visit}). \quad (5)$$

The base score follows an Upper Confidence Bound (UCB) formulation based on the GP posterior moments (μ_i, σ_i^2) , where the exploration weight β controls the trade-off between exploitation (high mean) and exploration (high uncertainty). The score is modulated by two heuristic factors: λ_i^{area} scales the reward proportionally to the node’s spatial area (ensuring fairness between macro and micro nodes), and the indicator function $\mathbb{I}(\cdot)$ acts as a binary filter that zeroes the reward of visited nodes.

The OP seeks a path π^* that maximizes the cumulative reward $\sum_{v_j \in \pi^*} r_j$ under a mission budget constraint. To map the temporal mission budget onto the spatial graph, we convert the remaining time T_{rem} into a distance budget $D_{rem} = T_{rem}/c$. Here, c acts as an amortized time-allocation factor that inherently inflates kinematic travel estimates, buffering sufficient margins for robot inter-region transits and intra-region tactical sampling. We solve this constrained OP efficiently using an Iterated Local Search heuristic initialized via randomized greedy selection [17].

Operating in a receding-horizon manner, the Global Planner extracts only the first target node $v_{next} \in \pi^*$ and its corresponding edge e_{next} . This edge dictates a tactical Local Time Budget $T_{local} = c \cdot \|e_{next}\|$. By passing the directive tuple (v_{next}, T_{local}) to the Local Planner, tactical maneuvers are bounded by strategic constraints, providing a stable execution horizon for information-rich maneuvers while preventing mission overtime. Global replanning is triggered when the robot reaches the region of the current target node v_{next} , decoupling high-level route planning from the high-frequency local control loop.

V. LOCAL PLANNING: UNIFIED RECEDING HORIZON INFORMATION SEARCH

Given the global directives (v_{next}, T_{local}) , the Local Planner generates a kinematically feasible, non-myopic trajectory towards v_{next} . It balances two objectives: (1) exploration: reducing map entropy via FLS/FLC scouting over both the substrate map \mathcal{B}^S and coral map \mathcal{B}^C , and (2) exploitation: precise DLC verification and targets sampling. To formulate this multi-sensor task as an efficient gradient-based Non-Linear Programming (NLP) problem, we propose a *Differentiable Belief Dynamics* framework. This deterministic surrogate models the expected evidence gain from stochastic observations as a continuous process, yielding smooth gradients that enable direct optimization of the robot’s control sequence to maximize information gain.

A. Multi-Modal Belief Snapshot & Candidate Identification

At each planning cycle t , the Local Planner initializes the optimization horizon by capturing a snapshot of the latest posterior beliefs \mathcal{B}_t^S and \mathcal{B}_t^C (updated via Eq. 3). These snapshot log-odds, ℓ_t^S and ℓ_t^C , serve as priors for the differentiable belief dynamics, thereby decoupling the evaluation of future information gain within the planning rollout from the online-evolving knowledge state. Concurrently, to direct the DLC's close-range sampling, we extract a discrete candidate map $\mathcal{M}_{samp} = \{m_i^{samp}\}_{i=1}^N$ from the coral belief \mathcal{B}_t^C . A cell i is flagged as a potential sampling target if its existence probability $P(c_i = 1)$ exceeds a confidence threshold δ :

$$m_i^{samp} = \mathbb{I}(P(c_i = 1) > \delta) = \mathbb{I}(\sigma(\ell_{t,i}^C) > \delta), \quad \forall i \in \mathcal{M},$$

where $\sigma(\cdot)$ denotes the logistic sigmoid mapping log-odds to probability.

B. Differentiable Belief Dynamics

The primary challenge in trajectory optimization is the incompatible nature of the sensor models: discrete FOV boundaries lack the smooth gradients necessary for NLP, while stochastic scouting (FLS/FLC) yields intractable entropy evolution. To resolve this, we formulate a deterministic surrogate model. Instead of predicting the exact stochastic posterior, it tracks expected accumulation of observation evidence, yielding continuous, differentiable information states.

For scouting modalities, the log-odds belief evolves as a random walk. Because active exploration fundamentally aims to push beliefs away from ambiguity ($l \approx 0$) regardless of the measurement outcome, we model the expected magnitude of this update. We define the *Accumulated Observation Confidence* $\Lambda \in [0, \infty)$ as a proxy state, initialized with the absolute log-odds snapshots: $\Lambda_{0,i}^{FLS} = |\ell_{t,i}^S|$ and $\Lambda_{0,i}^{FLC} = |\ell_{t,i}^C|$. Over the prediction horizon, Λ accumulates the sensor's *Average Evidence Magnitude* $\eta(d)$, which quantifies the expected log-odds increment per observation (effectively the Signal-to-Noise Ratio at observing distance d):

$$\eta(d) = \frac{1}{2} \left(\left| \log \frac{P_{TP}(d)}{P_{FP}(d)} \right| + \left| \log \frac{1 - P_{FP}(d)}{1 - P_{TP}(d)} \right| \right). \quad (6)$$

Therefore, the deterministic dynamics for both substrate (via FLS) and target beliefs (via FLC) can be formulated as:

$$\Lambda_{k+1,i}^{sensor} = \Lambda_{k,i}^{sensor} + \eta_{sensor}(d_{k,i}) \cdot \alpha_i^{sensor}(\mathbf{x}_k), \quad (7)$$

where α_i^{sensor} is a differentiable sensor field proxy that approximates the traditional binary observation indicator (i.e., 1 if observed, 0 otherwise), detailed in Sec. V-C). By maximizing Λ , the optimizer naturally drives the vehicle toward vantage points that yield high-SNR observations.

To integrate this accumulated evidence into the optimization cost, we map Λ to a proxy entropy H_{proxy} . Since Λ represents an optimistic upper bound on true stochastic confidence (via the triangle inequality $|l + \Delta l| \leq |l| + |\Delta l|$), it yields a lower-bound approximation of future uncertainty. We define $H_{proxy}(\Lambda)$ by converting Λ to a pseudo-probability $\hat{p} = \sigma(\Lambda)$ and applying the standard binary entropy formula:

$$H_{proxy}(\Lambda) = \ln(1 + e^\Lambda) - \Lambda \cdot \sigma(\Lambda). \quad (8)$$

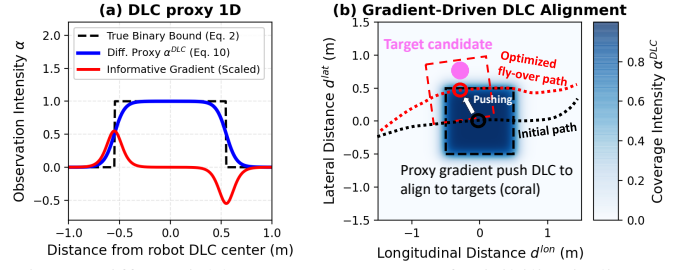


Fig. 4: Differentiable DLC proxy. (a) Soft visibility indicator α^{DLC} and gradient near the footprint boundary. (b) The resulting gradient steers the trajectory to align the footprint with target candidates.

This convex and monotonically decreasing surrogate provides consistent gradients to drive uncertainty reduction.

Conversely, for flagged candidate cells ($m_i^{samp} = 1$), we track a *Cumulative Verification Intensity* Λ^{down} —a proxy state representing the accumulated DLC coverage over the target. Its dynamics mirror Eq. 7 but utilize a constant, high information rate η_{down} for the DLC. We map Λ^{down} to a sampling probability via a saturation function:

$$P^{samp}(\Lambda_{k,i}^{down}) = 1 - \exp(-\lambda \cdot \Lambda_{k,i}^{down}). \quad (9)$$

This formulation enforces diminishing returns: as Λ^{down} grows, the vanishing gradient naturally prevents the robot from loitering over a sampled target, incentivizing efficient progression to subsequent candidates.

C. Differentiable Sensor Field Proxy

To enable gradient-based optimization, the soft visibility indicator at cell i , $\alpha_i(\mathbf{x}_t) \in [0, 1]$, of each sensor is modeled as a differentiable function of the robot state $\mathbf{x}_t = [\mathbf{p}_t^\top, \theta_t]^\top$ and cell coordinate \mathbf{p}_i . For FLS and FLC, we approximate their sector-shaped FOV (defined by maximum range R_{max} and half-angle β) using the product of sigmoids. Let $\Delta \mathbf{p}_{t,i} = \mathbf{p}_i - \mathbf{p}_t$ and $\phi_{t,i}$ be the relative bearing to the cell.

$$\alpha_i(\mathbf{x}_t) = \sigma(\gamma_d(R_{max} - \|\Delta \mathbf{p}_{t,i}\|)) \cdot \sigma(\gamma_a(\cos \phi_{t,i} - \cos \beta)),$$

where γ_d, γ_a control the boundary steepness. This yields two specific instantiated models: α^{FLS} and α^{FLC} .

Similarly, for the DLC with a square footprint of side L_{DLC} , we project the relative position $\Delta \mathbf{p}_{t,i}$ into the robot's body frame via the 2D rotation matrix $\mathbf{R}(\theta_t)$ to obtain the signed forward (longitudinal) and sideways (lateral) body-frame components: $[d_{t,i}^{lon}, d_{t,i}^{lat}]^\top = \mathbf{R}^\top(\theta_t) \Delta \mathbf{p}_{t,i}$. The soft footprint mask then smoothly approximates the hard square boundaries ($|d| \leq L_{DLC}/2$) via:

$$\alpha_i^{DLC}(\mathbf{x}_t) = \prod_{d \in \{d_{t,i}^{lon}, d_{t,i}^{lat}\}} \sigma\left(\frac{L_{DLC}/2 - |d|}{\epsilon}\right). \quad (10)$$

Unlike hard binary FOV boundaries that yield zero gradients outside the footprint, the proposed smooth proxy maintains a non-vanishing gradient in the vicinity of the boundary (Fig. 4a). During optimization, this gradient provides a consistent descent direction that pulls the vehicle state—both position and heading—toward configurations that better align the DLC footprint with target candidates (Fig. 4b).

D. Unified Optimization Formulation

We formulate the finite-horizon trajectory optimization as a monolithic NLP problem. Given the temporal budget T_{local} from the Global Planner, we define the horizon $H = \lfloor T_{\text{local}}/\Delta t \rfloor$. The Local Planner solves for an optimal finite-horizon control sequence $\mathbf{U}_{\text{local}}^* = \{\mathbf{u}_0, \dots, \mathbf{u}_{H-1}\}$, which induces the corresponding trajectory τ^* to minimize a unified cost function $J(\tau) = J_{\text{scout}} + J_{\text{samp}} + J_{\text{reg}}$, effectively trading off acoustic exploration, visual search, and target sampling against trajectory smoothness and control effort.

To drive multi-modal exploration, J_{scout} penalizes the negative expected entropy reduction for both the Substrate (\mathcal{B}^S) and Target beliefs (\mathcal{B}^C). For computational tractability, we evaluate this over a downsampled active map \mathcal{M}_{act} (obtained by pooling to form coarser map with the same spatial extent):

$$J_{\text{scout}} = - \sum_{k=0}^{H-1} \sum_{i \in \mathcal{M}_{\text{act}}} [w_s \Delta H(\Lambda_{k,i}^{\text{FLS}}) + w_c \Delta H(\Lambda_{k,i}^{\text{FLC}})],$$

where $\Delta H(\Lambda_{k,i}) = H_{\text{proxy}}(\Lambda_{k,i}) - H_{\text{proxy}}(\Lambda_{k+1,i})$. To ensure exploitation, J_{samp} drives DLC fly-overs by maximizing the expected sampling success over candidate map $\mathcal{M}_{\text{samp}}$:

$$J_{\text{samp}} = -w_{\text{samp}} \sum_{i \in \mathcal{M}_{\text{samp}}} m_i^{\text{samp}} \cdot P_{\text{samp}}(\Lambda_{H,i}^{\text{down}}).$$

Finally, J_{reg} enforces kinematic feasibility and smoothness via quadratic penalties on control energy and jerk, alongside a terminal cost to guide the robot toward the global waypoint v_{next} . The NLP is subject to system kinematics $\mathbf{x}_{k+1} = f(\mathbf{x}_k, \mathbf{u}_k)$, belief dynamics (Sec. V-B), and actuation limits. We discretize the problem via Direct Multiple Shooting and solve it using *CasADi* and *IPOPT* [18], [19], which efficiently exploits the sparsity of the belief dynamics to guarantee real-time, information-rich trajectory generation.

VI. EXPERIMENTS AND RESULTS

We evaluate HIMoS in a high-fidelity simulation environment derived from real-world UAV-based photogrammetry of shallow coral reefs shown in Fig. 5 [20]. We benchmark our approach against three baselines (key hyperparameters are summarized in Tab. I): *Boustrophedon* is a standard lawnmower-style exhaustive coverage strategy. *MCTS* represents the core non-myopic planning framework used in state-of-the-art coral sampling algorithms (e.g., SASS [8]), which we port to our fixed-altitude, multi-sensor setting to ensure a fair comparison. We also provide an upper-bound baseline *With Prior* that assumes access to the ground-truth substrate density map. It computes a global Orienteering Problem (OP) route offline using standard solvers, and executes using the same receding-horizon Local Planner as HIMoS.

A. Simulation Environment and Dataset

We utilize the Object-Based Image Analysis (OBIA) semantic segmentation maps from [20] as the simulation ground truth, inherently preserving the natural spatial clustering of benthic habitats. To create a planning-ready representation, the original semantic labels are rasterized into 0.25 m

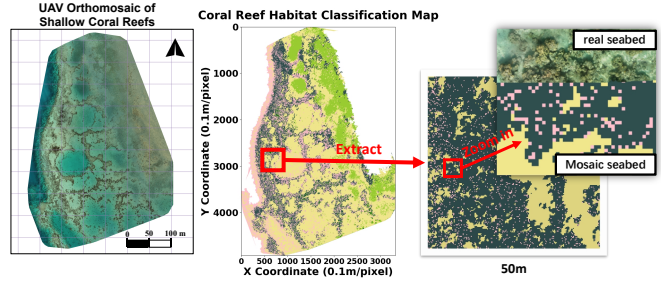


Fig. 5: Dataset-to-simulator pipeline.

TABLE I: Key experiment settings

| | |
|--------------------------|--|
| Robot | $v_{\text{max}} = 0.5 \text{ m/s}$, $\omega_{\text{max}} = 1.0 \text{ rad/s}$ |
| Planning | Frequency 2 Hz, $\Delta t = 0.5 \text{ sec}$ |
| MCTS action space | $\{[v, 0, 0], [0, \pm v, 0], [v_d, \pm v_d, 0], [v, 0, \pm \omega/2], [v, 0, \pm \omega]\}$ $v = 0.5 \text{ m/s}$, $\omega = 1.0 \text{ rad/s}$, $v_d = v/\sqrt{2}$ |
| HIMoS | |
| <i>Global planner</i> | Macro region = 4 m, Micro region = 2 m Empirical time-allocation factor $c = 6$ UCB exploration weight $\beta = 0.6$ |
| <i>Local planner:</i> | Weights $[w_{\text{sub}}, w_{\text{search}}, w_{\text{samp}}] = [1, 10, 5]$ Candidate threshold $\delta = 0.8$, execution steps $N_{\text{exec}} = 4$ |
| Sensor update | Frequency 2 Hz (two effective measurements per second) |
| FLS (substrate) | Range $R = 6.0 \text{ m}$, FOV 90° ; $P_{\text{TP}} = 1 - 0.1d_{\text{norm}}$, $P_{\text{FP}} = 0.1d_{\text{norm}}$ |
| FLC (target) | Range $R = 2.5 \text{ m}$, FOV 60° ; $P_{\text{TP}} = 1 - 0.15d_{\text{norm}}$, $P_{\text{FP}} = 0.15d_{\text{norm}}$ |
| DLC (verify) | Footprint $1.0 \times 1.0 \text{ m}$ (square) |

Note: $d_{\text{norm}} = d/R$ is the normalized distance, where d is the distance to the target and R is the corresponding sensor range.

$\times 0.25 \text{ m}$ grid cells. We consolidate the diverse benthic classes into three task-relevant categories: *sand*, *hard substrate*, and *coral*. Because the original annotations provide habitat-level boundaries rather than discrete target locations, we instantiate individual coral targets by probabilistically sampling cells within the coral-labeled regions. This process yields discrete, sparsely distributed targets while rigorously maintaining the authentic spatial layout of the seabed.

For systematic benchmarking, we extract 12 distinct $50 \text{ m} \times 50 \text{ m}$ sub-maps from the global survey area. As shown in Fig. 6, these maps exhibit substantial variation in coral prevalence and substrate clustering. To thoroughly evaluate algorithmic robustness, we categorize these sub-maps into *easy*, *medium*, and *hard* subsets based on target counts and the spatial fragmentation of the hard substrates.

B. Performance Analysis

To systematically evaluate algorithmic robustness, we conduct 48 independent runs per baseline by varying starting locations across the 12 maps. Fig. 8(a-c) presents the target confirmation ratio (percentage of sampled targets) over a 2000 s budget. HIMoS consistently outperforms both *MCTS* and *Boustrophedon* across all difficulty levels. Remark-

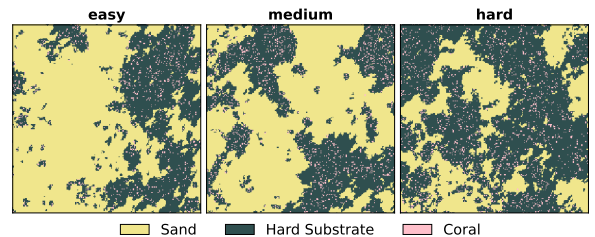


Fig. 6: Representative test maps ($50 \text{ m} \times 50 \text{ m}$).

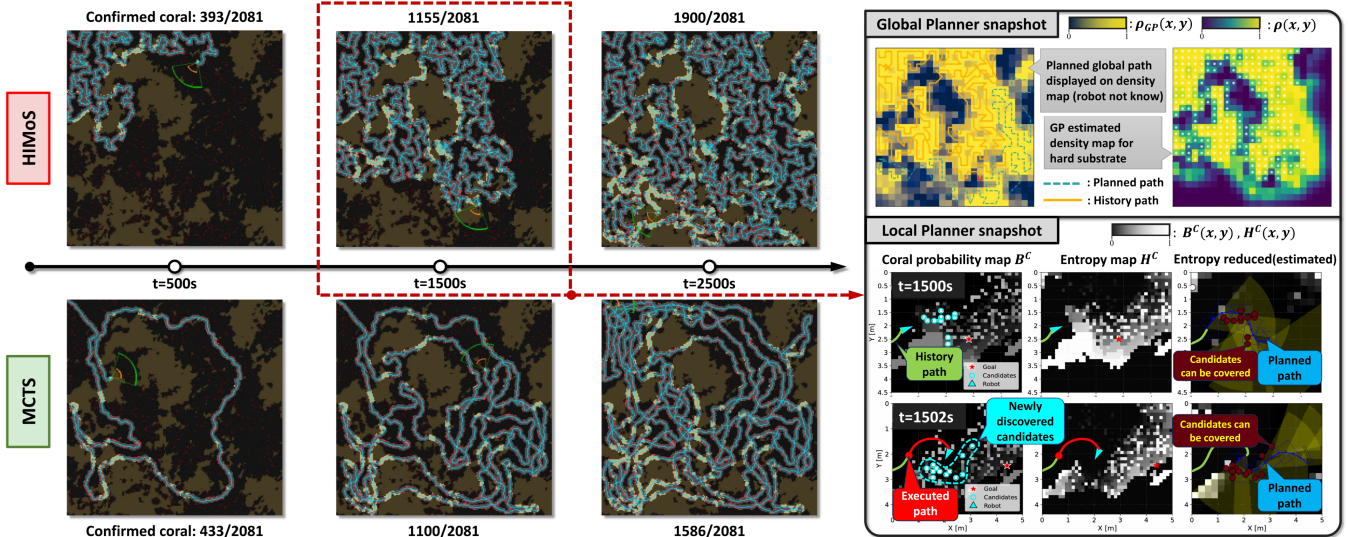


Fig. 7: Qualitative trajectory analysis. Left: trajectory evolution for HIMoS and MCTS at 500/1500/2500 s. Right: HIMoS planning snapshots at 1500 s, showing the Global Planner (top) and Local Planner (bottom).

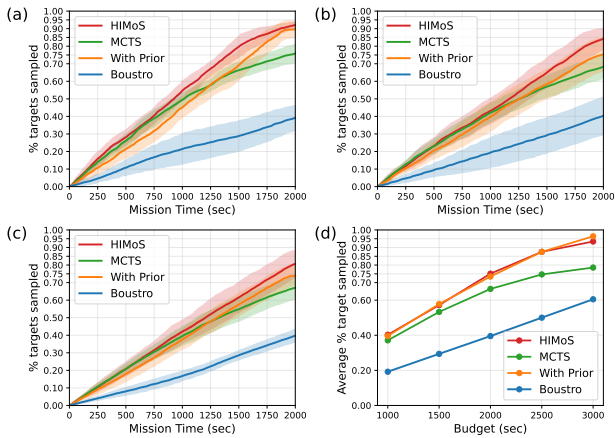


Fig. 8: (a-c) Sampling ratio vs. mission time under a fixed 2000 s budget across *easy*, *medium*, and *hard* environments. Solid curves denote the mean, with shaded areas indicating standard deviation. (d) Average final ratio across varying time budget in the two hardest scenarios

ably, HIMoS achieves a marginally higher confirmation rate than the *With Prior* baseline, despite lacking initial environmental knowledge. This counter-intuitive result highlights a fundamental limitation of offline planning: solving the OP over an entire dense map suffers from the curse of dimensionality, yielding sub-optimal open-loop routes even given generous computation time (100 s). In contrast, HIMoS dynamically decomposes the massive OP into tractable sub-problems via its adaptive multi-resolution graph, continuously refining the global strategy with recent evidence.

Also, the temporal curves reveal diminishing marginal utility in the baselines. While MCTS is competitive early on, its discovery rate plateaus after 1500 s. Evaluating performance under varying mission budgets (1000 s to 3000 s) on the two hardest maps (Fig. 8d) further illustrates this. MCTS shows marginal gains after 2000 s, whereas HIMoS maintains a high and steady confirmation rate across different budgets. The

underlying kinematic behaviors and planning logic driving this performance gap are detailed in Sec VI-C.

C. Trajectory Behavior Analysis

To illustrate the underlying planning behaviors, we visualize a 2500 s mission on a challenging map. Fig. 7 (left) compares the trajectory evolution. Initially at 500 s, MCTS explores aggressively, yielding a higher sample count than HIMoS (433 vs. 393). However, under a strict 0.5 s rollout limit to maintain 2Hz planning, the large branching factor causes the search tree to grow exponentially with depth, which in turn truncates the practical look-ahead horizon. Lacking global structure, MCTS struggles to identify distant unvisited habitats once a local region is depleted. Consequently, by 2500 s, it wastes energy traversing previously swept areas, stalling at a 76% confirmation rate.

Conversely, HIMoS exhibits deliberate, region-by-region exploration and exploitation, ultimately achieving a 91% confirmation rate. As shown in the Global Planner snapshot at 1500 s (Fig. 7, top right), HIMoS continuously regresses acoustic observations into a substrate density map. This enables a strategic, long-horizon topological skeleton that efficiently bridges unvisited high-probability rocky habitats, fundamentally preventing redundant traversals.

Guided by the latest global waypoint (red star), the Local Planner orchestrates tactical maneuvers (Fig. 7, lower right)². Driven by the differentiable belief dynamics, the solver generates smooth, non-myopic trajectories that deviate from the topological edge to maximize information gain. The planner actively directs its FLC (yellow sector) toward high-entropy regions in its belief map B^C (white areas) while concurrently aligning the vehicle to sweep its DLC footprint (blue dashed squares) directly over high-probability coral candidates (cyan circles). Executing in a receding-horizon

²The FLS sector and substrate belief and entropy map are omitted for visual clarity.

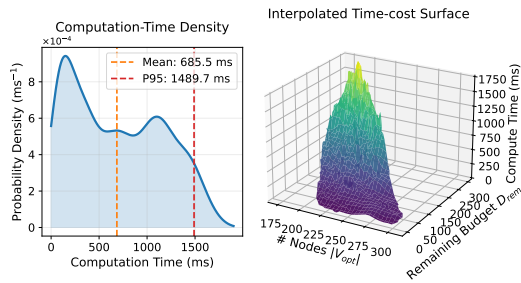


Fig. 9: Global Planner computation cost. Left: Solve-time distribution. Right: Time-cost surface w.r.t. number of active nodes \mathcal{V}_{opt} and remaining budget D_{rem} .

manner ($N_{exec} = 4$), HIMoS seamlessly incorporates new observations to update the belief map—as evidenced by the newly discovered candidates at 1502s—and replans the subsequent trajectory, successfully balancing broad-area information gathering with biological target sampling.

D. Computational Cost Analysis

Real-time performance is critical for embedded AUVs. Although the current implementation is an unoptimized Python prototype, experiments on a Jetson AGX Orin show that the Local Planner solves the NLP in 0.5 s on average. Executing $N_{exec} = 4$ steps provides a 2.0 s execution horizon, masking computation latency. For the Global Planner, OP runtime scales with active nodes and remaining budget (Fig. 9). Because replanning is event-triggered upon reaching a target region, updates are infrequent. With 95% of global calls finishing within 1.5 s, HIMoS supports real-time deployment.

VII. CONCLUSION

We presented HIMoS, a hierarchical multi-modal informative planning framework for fixed-altitude sparse target search. By integrating an adaptive orienteering Global Planner with this local trajectory optimization, HIMoS seamlessly balances wide-area acoustic exploration, visual scouting, and precise target sampling. Our differentiable belief dynamics is a general formulation applicable to any probabilistic sensor model given a spatial FOV. Evaluated on real-world benthic datasets with sensor settings reflecting real deployment conditions, the algorithm delivers efficient, robust real-time performance on an embedded AUV computer, indicating strong sim-to-real readiness. While the current global-to-local budget conversion employs a coarse linear heuristic, future work will investigate a rigorous, dynamics-aware allocation mechanism and fully deploy HIMoS on a physical AUV for real-world ocean monitoring missions.

REFERENCES

- [1] A. Sultan, L. S. Saoud, M. Elmezain, M. Heshmat, L. Seneviratne, and I. Hussain, “Autonomous robotic systems for coral reef monitoring: Review and open research issues,” *Ecological Informatics*, p. 103511, 2025.
- [2] L. Chen, S. Kailas, S. Deolasee, W. Luo, K. Sycara, and W. Kim, “Distributed multi-robot source seeking in unknown environments with unknown number of sources,” in *2025 IEEE International Conference on Robotics and Automation (ICRA)*, IEEE, 2025, pp. 7335–7341.

- [3] R. Marchant and F. Ramos, “Bayesian optimisation for informative continuous path planning,” in *2014 IEEE International Conference on Robotics and Automation (ICRA)*, IEEE, 2014, pp. 6136–6143.
- [4] E. Galceran and M. Carreras, “A survey on coverage path planning for robotics,” *Robotics and Autonomous systems*, vol. 61, no. 12, pp. 1258–1276, 2013.
- [5] K.-C. Huang, F.-L. Lian, C.-T. Chen, C.-H. Wu, and C.-C. Chen, “A novel solution with rapid voronoi-based coverage path planning in irregular environment for robotic mowing systems,” *International Journal of Intelligent Robotics and Applications*, vol. 5, no. 4, pp. 558–575, 2021.
- [6] Z. Zheng, Y. Liu, H. Wang, and Z. Ren, “Ergodic trajectory planning with dynamic sensor footprints,” *arXiv preprint arXiv:2512.08661*, 2025.
- [7] A. A. Meera, M. Popović, A. Millane, and R. Siegwart, “Obstacle-aware adaptive informative path planning for uav-based target search,” in *2019 International Conference on Robotics and Automation (ICRA)*, IEEE, 2019, pp. 718–724.
- [8] J. E. Todd, S. McCammon, Y. Girdhar, N. Roy, and D. Yoerger, “Adaptive multi-altitude search and sampling of sparsely distributed natural phenomena,” pp. 8650–8657, 2024. DOI: 10.1109/IROS58592.2024.10802325
- [9] F. F. Sørensen, C. Mai, O. M. Olsen, J. Liniger, and S. Pederesen, “Commercial optical and acoustic sensor performances under varying turbidity, illumination, and target distances,” *Sensors*, vol. 23, no. 14, p. 6575, 2023.
- [10] L. Chen, J. Tang, A. P.-Y. Chui, Z. Hong, and J. Wu, “Sonar-sweep: Fusing sonar and vision for robust 3d reconstruction via plane sweeping,” *arXiv preprint arXiv:2511.00392*, 2025.
- [11] R. V. Garone, T. I. Birkenes Lønmo, A. C. G. Schimel, M. Diesing, T. Thorsnes, and L. Løvstakken, “Seabed classification of multibeam echosounder data into bedrock/non-bedrock using deep learning,” *Frontiers in Earth Science*, vol. 11, p. 1285368, 2023.
- [12] W. Xu, J. Yang, H. Wei, H. Lu, X. Tian, and X. Li, “Seabed mapping for deep-sea mining vehicles based on forward-looking sonar,” *Ocean Engineering*, vol. 299, p. 117276, 2024.
- [13] W. J. Wright, K. M. Irvine, T. J. Rodhouse, and A. R. Litt, “Spatial gaussian processes improve multi-species occupancy models when range boundaries are uncertain and nonoverlapping,” *Ecology and Evolution*, vol. 11, no. 13, pp. 8516–8527, 2021.
- [14] S. Thrun, “Probabilistic robotics,” *Communications of the ACM*, vol. 45, no. 3, pp. 52–57, 2002.
- [15] C. E. Rasmussen, “Gaussian processes in machine learning,” in *Summer school on machine learning*, Springer, 2003, pp. 63–71.
- [16] P. Vansteenwegen, W. Souffriau, and D. Van Oudhekste, “The orienteering problem: A survey,” *European Journal of Operational Research*, vol. 209, no. 1, pp. 1–10, 2011.
- [17] T. A. Feo and M. G. Resende, “Greedy randomized adaptive search procedures,” *Journal of global optimization*, vol. 6, no. 2, pp. 109–133, 1995.
- [18] A. Wächter and L. T. Biegler, “On the implementation of an interior-point filter line-search algorithm for large-scale nonlinear programming,” *Mathematical programming*, vol. 106, no. 1, pp. 25–57, 2006.
- [19] J. A. Andersson, J. Gillis, G. Horn, J. B. Rawlings, and M. Diehl, “Casadi: A software framework for nonlinear optimization and optimal control,” *Mathematical Programming Computation*, vol. 11, no. 1, pp. 1–36, 2019.
- [20] B. O. Nieuwenhuis, P. Visser, B. Lewis, et al., “Integrating a uav-derived dem in object-based image analysis increases habitat classification accuracy on coral reefs,” *Remote Sensing*, 2022.